

Cold atomic beam ion source for focused ion beam applications

B. Knuffman,^{1,2,3} A. V. Steele,^{1,2,3,a)} and J. J. McClelland¹

¹Center for Nanoscale Science and Technology, National Institute of Standards and Technology, Gaithersburg, Maryland 20899, USA

²Maryland Nanocenter, University of Maryland, College Park, Maryland 20742, USA

³zeroK NanoTech, Montgomery Village, Maryland 20886, USA

(Received 13 May 2013; accepted 19 June 2013; published online 23 July 2013)

We report measurements and modeling of an ion source that is based on ionization of a laser-cooled atomic beam. We show a high brightness and a low energy spread, suitable for use in next-generation, high-resolution focused ion beam systems. Our measurements of total ion current as a function of ionization conditions support an analytical model that also predicts the cross-sectional current density and spatial distribution of ions created in the source. The model predicts a peak brightness of $2 \times 10^7 \text{ A m}^{-2} \text{ sr}^{-1} \text{ eV}^{-1}$ and an energy spread less than 0.34 eV. The model is also combined with Monte-Carlo simulations of the inter-ion Coulomb forces to show that the source can be operated at several picoamperes with a brightness above $1 \times 10^7 \text{ A m}^{-2} \text{ sr}^{-1} \text{ eV}^{-1}$. We estimate that when combined with a conventional ion focusing column, an ion source with these properties could focus a 1 pA beam into a spot smaller than 1 nm. A total current greater than 5 nA was measured in a lower-brightness configuration of the ion source, demonstrating the possibility of a high current mode of operation. © 2013 Author(s). All article content, except where otherwise noted, is licensed under a Creative Commons Attribution 3.0 Unported License. [<http://dx.doi.org/10.1063/1.4816248>]

I. INTRODUCTION

Focused ion beams (FIBs) are used for a variety of nanomachining, sample preparation, and sample analysis tasks. Modern FIBs are able to remove material at the nanoscale through sputtering, or add material through beam-activated chemistry when used with a precursor gas.¹ FIBs also enable spatially resolved elemental analysis using secondary ion mass spectrometry (SIMS),² as well as high-resolution imaging with unique contrast and surface sensitivity capabilities.³ Since the performance of FIBs is determined primarily by the system's ion source, a new source that provides increased brightness, reduced energy spread, and an ionic species that minimizes sub-surface damage is highly desirable.

The most commonly used FIB ion source today is the liquid metal ion source (LMIS). With a brightness⁴ of $10^6 \text{ A m}^{-2} \text{ sr}^{-1} \text{ eV}^{-1}$ and an energy spread of a few electron volts,⁵ the LMIS can deliver approximately 1 pA into a 5 nm to 10 nm spot at a 30 keV beam energy. The LMIS can also provide a few tens of nanoamperes into a wider area for larger scale material removal. The gallium LMIS is the most commonly used because of its simplicity and robustness, although gallium ions are not ideal for a number of applications because of their tendency to contaminate or otherwise destroy the sample. Another source that performs very well in imaging applications is the gas field ion source (GFIS),⁶ which produces a few-picoampere helium ion beam that can be focused to a sub-nanometer probe size.

Recently, a new type of ion source that makes use of photoionized, laser-cooled gasses has emerged, promising high

brightness, low energy spread, and a wide choice of ionic species. Several proposals for such a source have been discussed,^{7–9} and realizations, referred to as a magneto-optical trap ion source (MOTIS) or ultracold ion source (UCIS), have been described.^{10,11} Complete FIB systems with chromium¹² and lithium ions¹³ have also been constructed.

In a laser-cooled photoionization source, the high brightness is achieved through the extraordinarily cold, microkelvin-range temperatures attainable through laser cooling. These cold temperatures result in a very small angular spread in the ion beam, making possible a high brightness without shrinking the source size to very small dimensions. However, there is a disadvantage when a magneto-optical trap (MOT) is used in the ion source. As discussed in Ref. 14, a low temperature in the MOT results in a low diffusion rate for the cold atoms, limiting the rate at which the ionization region can be refilled with neutral atoms as ion current is created. The resulting trade-off between low angular spread and beam current imposes a brightness limit on this type of ion source.

Here, we present results from measurements and modeling of a laser-cooled ion source that may offer improved performance for precision nanomachining and fabrication work. The design avoids the brightness limitations of the MOTIS by ionizing a cold, slow atomic beam that is transversely compressed and cooled to microkelvin temperatures. Providing a steady flux of neutral atoms avoids the diffusion limit, allowing much higher ion currents, while laser cooling in the transverse direction provides the cold temperatures necessary for a high brightness, as long as the atom beam axis is well-aligned with the ion beam axis. Cesium was chosen for our demonstration because it is the heaviest of the easily laser-coolable atomic species, yielding efficient sputtering and minimizing lateral straggle damage and range in

^{a)}Author to whom correspondence should be addressed. Electronic mail: adam@zerok.com



many target materials. It also may offer additional analytical capabilities by improving the performance of site-specific SIMS.¹⁵

II. EXPERIMENT

The creation of a high-flux, neutral atomic beam by laser cooling and compression has been discussed in the literature previously.^{16–18} In our system, shown schematically in Figure 1, a slow atomic beam is generated by combining a two-dimensional MOT with a retroreflected laser beam along the third axis (pusher beam). The pusher beam imparts momentum to the cold atoms along the axis of the 2D-MOT, creating a beam of atoms with reasonably well-defined velocity which exits through a small hole in the retroreflecting mirror. This configuration has been referred to as a 2D⁺-MOT,¹⁹ and is similar to a “low velocity intense source” (LVIS).²⁰ The chamber containing the 2D⁺-MOT is filled with cesium vapor. In our realization, the atomic beam from this source has a total integrated flux of up to $5 \times 10^{10} \text{ s}^{-1}$, a transverse temperature of typically 5 mK, and a mean axial velocity between 6 m/s and 14 m/s depending on the power used in the pusher beam. These beam parameters were measured by observing absorption and fluorescence from an on-resonance probe laser beam. We note that the kinetic energy associated with the axial velocity of the beam amounts to about 70 μeV , and hence contributes negligibly to the energy of the ion beam.

In order to increase the intensity of the atomic beam, we use a magneto-optical compressor (MOC)¹⁶ to capture the beam produced by the 2D⁺-MOT and reduce its radial size. The MOC is a 2D-MOT with a magnetic field gradient that increases along the atom beam axis. Inside our MOC the peak

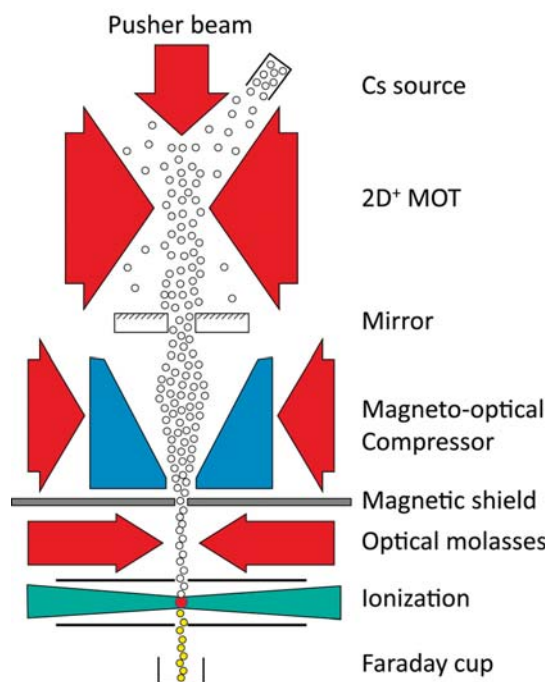


FIG. 1. Schematic of the cold atomic beam ion source, showing the four stages of ion beam production: 2D magneto-optical trap with pusher beam (2D⁺-MOT), magneto-optical compressor, optical molasses, and ionization.

field gradient is approximately 0.5 T/m. By imaging the fluorescence from a probe laser beam crossing the atom beam at the exit of the MOC, we found that atoms are captured into the MOC with near unit efficiency, and the beam has a nearly Gaussian density distribution with a one-sigma radius of approximately 60 μm along both axes. Observing the fluorescence at two locations along the beam allowed us to determine the transverse temperature of the atoms exiting the MOC, and this was found to be between 100 μK and 150 μK depending on the detuning and total power used in the MOC beams.

To further reduce the transverse temperature, we apply a two-dimensional $\sigma^+ - \sigma^-$ optical molasses²¹ to the atomic beam exiting the MOC. Because stray magnetic fields can reduce the cooling efficiency of optical molasses, our system includes a sheet of high-magnetic-permeability material placed directly after the MOC. This shielding diverts the magnetic field lines emerging from the MOC, creating a nearly field-free region. Measurements on the atomic beam emerging from the optical molasses showed a temperature of $(30 \pm 10) \mu\text{K}$.²² This measurement has a large uncertainty because at these temperatures the atomic beam spreads very slowly as a function of axial position, making the distance required to observe appreciable broadening very long. The length of our vacuum chamber prevented a more precise measurement. Additionally, the temperatures for the two transverse axes were not precisely the same, and the measured temperature was found to be highly sensitive to small changes in the axial position of the molasses beams. We believe that this sensitivity is due to residual stray magnetic fields from the MOC interfering with the operation of the molasses.

The compressed, cooled atomic beam next enters the ionization region which is bounded by two flat plates with apertures. Potentials applied to the plates create a nearly uniform electric field which accelerates ions through the aperture in the lower plate and into a Faraday cup. Between the plates, two crossed laser beams are tightly focused with their foci overlapping at the center of the atomic beam (see Figure 2). One laser is tuned to the Cs $6S_{1/2} (F=4) - 6P_{3/2} (F=5)$ cycling transition near 852 nm and has a one-standard-deviation radius of $(2.25 \pm 0.20) \mu\text{m}$. The other beam is tuned near 508 nm and

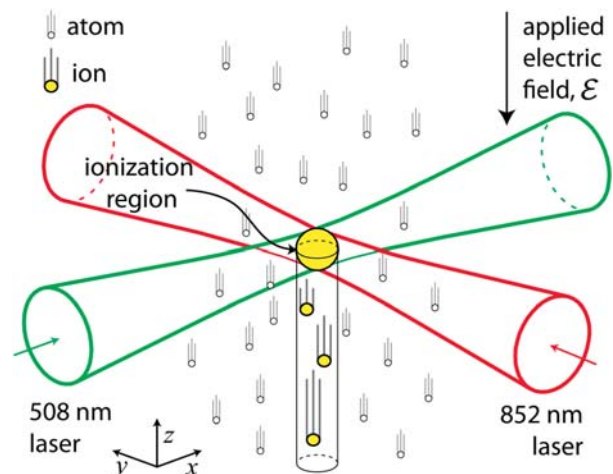


FIG. 2. Ionization laser geometry, showing the overlapping 852 nm resonant driving laser and 508 nm ionization laser.

has a one-standard-deviation radius of $(1.75 \pm 0.20) \mu\text{m}$. The 508 nm beam photoionizes the atoms by driving them from the upper state of the cycling transition to just above the ionization threshold, creating ions with minimal additional heating. We note that the two lasers can also be intentionally defocused so that their overlap volume is larger, making a larger beam with more ion current. The spatial profiles and power levels of these laser beams were characterized using scanning-slit and calibrated-photodiode measurements. We also measured the saturation intensity for the 852 nm cycling transition, using an absorption measurement of the laser passing through the atomic beam. The saturation intensity value is needed for the model as described below.

III. MODEL

In order to predict the suitability of an ion source for high-resolution focusing, the most important parameters are the normalized brightness and the energy spread. Together with knowledge of the aberration coefficients of the focusing optics, these allow us to estimate attainable values of the spot size and current. However, when an ion source has a high brightness, direct measurement becomes quite difficult because it is challenging to measure the small angular divergences characteristic of these laser-cooled sources. To arrive at estimates of the ion beam brightness in our source we have chosen to rely on a combination of measurements performed on the atomic beam and ionization lasers, measurements of the total ion current, and detailed modeling of the ionization process and beam formation, including the effects of Coulomb interactions between the ions. Because the processes of laser excitation and ionization of isolated neutral atoms are well-understood,²³ and because the measurements involved are the sort that can be performed with good accuracy and precision, we expect our modeling to generate good predictions of brightness and energy spread. Comparisons of model predictions for total beam current as a function of excitation and ionization laser powers provide confidence that the modeling is correct.

The model, with no adjustable parameters, takes as input the measured neutral atom beam geometry and flux together with the ionization laser beam intensity distributions and predicts the three-dimensional ion current density distribution $J(x, y, z)$. The integration of this distribution over the transverse coordinates x and y yields the total current in the beam at a point z , which is then compared with the observed current as a test of the model. We note that the total current is a function of z because ions are being created as the neutral atoms pass through the ionization region. The current density distribution is also used to derive the ion current creation probability density $P(x, y, z)$, which is then input into a Monte-Carlo calculation of the inter-ion Coulomb interactions, making it possible to predict any deleterious effects on the brightness at high beam currents. $P(x, y, z)$ also allows us to calculate where in the potential ions are created, and thus to determine the distribution of ion kinetic energies in the beam after acceleration.

The model begins with the assumption that the neutral atom beam entering the ionization volume is well approximated

by a collimated Gaussian beam propagating in the z -direction. This assumption is consistent with our observations of the atomic beam, and is appropriate given the low transverse temperature of the atomic beam and the relatively short z -extent of the ionization volume. We write the initial neutral atom flux $\Phi_0(x, y)$ in terms of the integrated flux F and the standard deviation σ_A as

$$\Phi_0(x, y) = \frac{F}{2\pi\sigma_A^2} \exp\left\{-\frac{x^2 + y^2}{2\sigma_A^2}\right\}. \quad (1)$$

With the assumption of perfect collimation, we can treat the ionization process as a quasi-one-dimensional problem, with neutral atoms entering the ionization region and eventually being converted to ions with some integrated probability as they travel along z . With a further assumption that all atoms travel with a single velocity v , justified because the atomic beam in our source has a velocity spread $\Delta v/v$ of approximately 0.2 or less, we can write a differential equation for the ion beam current density

$$\frac{dJ(x, y, z)}{dz} = \frac{e}{v} R_{\text{ion}}(x, y, z) \Phi(x, y, z), \quad (2)$$

where e is the electric charge, $R_{\text{ion}}(x, y, z)$ is the spatially dependent ionization rate, and $\Phi(x, y, z)$ is the neutral atom flux, which has a z -dependence because the ionization process depletes the neutral atom beam as it propagates. Conservation of particles allows us to write the neutral atom flux as

$$\Phi(x, y, z) = \Phi_0(x, y) - \frac{1}{e} J(x, y, z), \quad (3)$$

which then permits the integration of Eq. (2) to yield

$$J(x, y, z) = \frac{eF}{2\pi\sigma_A^2} \exp\left\{-\frac{x^2 + y^2}{2\sigma_A^2}\right\} \times \left(1 - \exp\left\{-\frac{1}{v} \int_{-\infty}^z R_{\text{ion}}(x, y, z') dz'\right\}\right). \quad (4)$$

In the absence of Coulomb interactions, the normalized brightness of the ion beam can be derived directly from this expression via

$$B(x, y) = \frac{J(x, y, +\infty)}{\pi k_B T}, \quad (5)$$

where k_B is Boltzmann's constant and T is the transverse temperature of the atomic beam.²⁴

The spatially dependent ionization rate $R_{\text{ion}}(x, y, z)$ is modeled by a two-photon process in which a first laser couples the neutral Cs atomic ground state to an intermediate state creating an average excited state fraction $\rho_e(x, y, z)$, and a second laser then ionizes atoms in the intermediate state at a rate $\tilde{R}_{\text{ion}}(x, y, z)$. The overall photoionization rate is the product

$$R_{\text{ion}}(x, y, z) = \rho_e(x, y, z) \tilde{R}_{\text{ion}}(x, y, z). \quad (6)$$

Because the relaxation rate of the intermediate state population is very fast (30 ns) compared with the transit time of an atom through the ionization volume, we can assume quasi-steady state conditions, and the excited state fraction can be expressed in terms of the intensity of the resonant driving laser field I_1 and the saturation intensity I_s as

$$\rho_e(x, y, z) = \frac{1}{2} \frac{I_1(x, y, z)/I_s}{1 + I_1(x, y, z)/I_s}. \quad (7)$$

The rate of ionization from the intermediate state to the continuum can be written in terms of the ionization cross section σ_{ion} and the intensity of the ionizing laser I_2 as

$$\tilde{R}_{\text{ion}}(x, y, z) = \frac{\sigma_{\text{ion}} \lambda_2}{hc} I_2(x, y, z), \quad (8)$$

where λ_2 is the wavelength of the ionizing laser, h is Planck's constant, and c is the speed of light. The near-threshold ionization cross section was taken from measured literature values.^{25,26} The overall ionization rate R_{ion} depends on the spatial distribution of the light intensity in the two lasers and is only nonzero in regions of overlap. For the purposes of the model, the two lasers were assumed to be focused Gaussian laser beams with perfectly overlapped foci, in which case the intensities can be written as

$$I_1(x, y, z) = \frac{P_1}{2\pi\sigma_1^2 \left(1 + \frac{y^2}{l_{R1}^2}\right)} \exp\left\{-\frac{x^2 + z^2}{2\sigma_1^2 \left(1 + \frac{y^2}{l_{R1}^2}\right)}\right\}, \quad (9)$$

$$I_2(x, y, z) = \frac{P_2}{2\pi\sigma_2^2 \left(1 + \frac{x^2}{l_{R2}^2}\right)} \exp\left\{-\frac{y^2 + z^2}{2\sigma_2^2 \left(1 + \frac{x^2}{l_{R2}^2}\right)}\right\}, \quad (10)$$

where P_1 and P_2 are the total laser powers, σ_1 and σ_2 are the standard deviations, and $l_{R1} = 4\pi\sigma_1^2/\lambda_1$ and $l_{R2} = 4\pi\sigma_2^2/\lambda_2$ are the Rayleigh lengths for the two laser beams.

Given the current density distribution in the ion beam $J(x, y, z)$, it is also useful to have the spatially dependent ion current creation probability density $P(x, y, z)$. This quantity can be derived by noting that it is equal to the derivative of $J(x, y, z)$ with respect to the z -coordinate

$$P(x, y, z) = \frac{dJ(x, y, z)}{dz}. \quad (11)$$

$P(x, y, z)$ can be associated with the amount of current created at a point (x, y, z) in an infinitesimal volume $dx dy dz$. It is helpful for three-dimensional visualization of the ion source's ionization volume, as shown in Figure 3, and is also what is needed as input into Monte Carlo calculations of inter-ion Coulomb interactions, as discussed below.

The energy spread in the beam is obtained by integrating $P(x, y, z)$ over x and y to yield a z -dependent distribution of

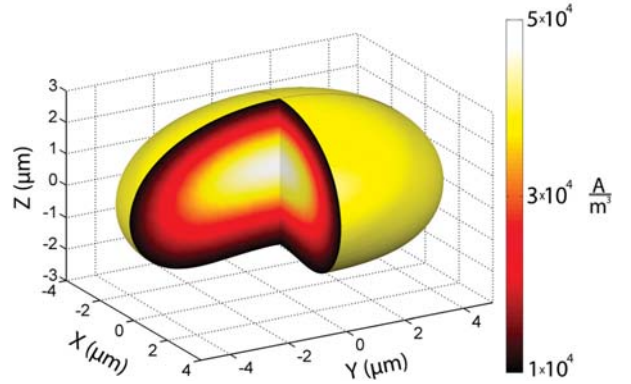


FIG. 3. Ionization volume, as determined by the spatially dependent ion current creation probability density $P(x, y, z)$. Calculation was done with the parameters in Table I. The outer shell represents a constant surface $P(x, y, z) = 1 \times 10^4 \text{ A/m}^3$.

created ion current $P_I(z)$. In our ion source the longitudinal temperature of the ions arising from the velocity spread in the ion beam is less than $10 \mu\text{eV}$, and so contributes negligibly to the energy spread in the ion beam. Instead, the energy distribution $P_E(E)$ is primarily determined by the fact that ions are created over a finite spatial extent in a uniform electric field \mathcal{E} . Thus $P_E(E)$ can be calculated from $P_I(z)$ using the fact that the final energy of an ion will be $E = E_0 + e\mathcal{E}z$, where E_0 is the energy of ions that start at $z = 0$, the center of the ionization volume. Transforming the coordinate from z to E gives

$$P_E(E) = \frac{1}{e\mathcal{E}} \frac{P_I\left(\frac{E - E_0}{e\mathcal{E}}\right)}{I_{\text{ion}}}, \quad (12)$$

where the factor of $1/I_{\text{ion}}$ has been added for normalization, with I_{ion} being the total ion current.

To obtain numerical predictions from the model, we chose input parameter values corresponding to experimental conditions, and these are summarized in Table I. Using these values, we obtain from the model a peak current density $J(0, 0, +\infty)$ of 0.16 A m^{-2} . Assuming that the temperature of the ion beam is the same as the underlying atomic beam, $30 \mu\text{K}$, we use Eq. (5) to calculate a peak brightness of $2 \times 10^7 \text{ A m}^{-2} \text{ sr}^{-1} \text{ eV}^{-1}$. We note that our assumption of

TABLE I. Numerical values for the parameters used as input to the model in calculating the ion current creation probability shown in Figure 3. All parameters represent measured quantities taken directly from the experiment, with the exception of σ_{ion} , which was obtained from the literature.

Symbol	Definition	Value
F	Integrated atom flux	$4.7 \times 10^{10} \text{ s}^{-1}$
σ_A	Atom beam radius (one sigma)	$84 \mu\text{m}$
P_1	852 nm laser power	2 nW
σ_1	852 nm laser focus radius (one sigma)	$2.25 \mu\text{m}$
P_2	508 nm laser power	125 mW
σ_2	508 nm laser focus radius (one sigma)	$1.75 \mu\text{m}$
I_s	$6S_{1/2} \rightarrow 6P_{3/2}$ saturation intensity	62 W m^{-2}
v	Atom beam velocity	11 m s^{-1}
σ_{ion}	$6P_{3/2}$ ionization cross-section	$2 \times 10^{-21} \text{ m}^2$

equal atom and ion temperatures should be good as long as the ionization laser frequency is kept close to the ionization threshold and is consistent with previous brightness measurements made on a similar laser-cooled ion source.¹³ However, this assumption does merit further investigation.

A numerical value for the energy spread can be derived from Eq. (12) with the assumption of a value for the extraction electric field \mathcal{E} . While choosing a lower value will always give a smaller energy spread, a larger value may be necessary to keep Coulomb interaction effects to a minimum, depending on the desired beam current.²⁷ Based on a desired current of 1 pA to 2 pA and considering our Monte Carlo simulations discussed below, we have chosen an extraction field of 100 kV/m. With this field, which is easily obtained in a practical realization of the source, we find a full-width at half maximum energy spread of $\Delta E = 0.34$ eV. This is significantly smaller than the energy spread of a few electron volts typical of the LMIS and compares favorably with the estimated 0.5 eV spread of the GFIS at 20 keV.⁶

IV. RESULTS

With the aim of validating our model, we conducted a series of measurements on the total ion current produced by the source as a function of the laser powers in the 852 nm (P_1) and 508 nm (P_2) beams. Measurements and corresponding model predictions are shown in Figure 4. We estimate the uncertainty in the current measurements to be approximately 5% (one standard deviation) of the measured value, arising predominantly from minor random variations in laser intensity and positional stability. Figure 4(a) shows the dependence of the ion current on the ionization laser power P_2 at several values of the resonant driving laser power P_1 . As seen in the figure, for low values of P_1 (1 nW and 2 nW) the model shows excellent agreement with the measurements, indicating that it is capturing the most significant aspects of the ionization process. At the higher values of P_1 , 10 nW and 100 nW, the model shows some deviation from the measurements. We believe that this deviation is due to photon rescattering effects. At higher values of P_1 , a significant population of excited-state atoms will exist for some distance along the axis of the resonant driving laser. These atoms will re-radiate resonant light, which will be absorbed by other atoms in the incident atom beam, creating significant excited state population in regions outside the overlap volume. Some of this excited state population will lie in the path of the ionization laser, where it will be ionized, resulting in additional current in the beam that does not originate in the ionization volume.

To investigate the possibility of rescattering, we performed additional measurements in which the two lasers were offset vertically by a few microns so that they were no longer overlapping. In this configuration, any current that is observed will be created solely by rescattering. Because the two lasers remain in close proximity, the total amount of rescattered photons resulting in spurious ion current should be nearly the same as in the overlap case. The results of these measurements are shown in Figure 4(b). The fact that we observed several picoamperes of current even though the beams were not overlapping is a good indication that rescattering was

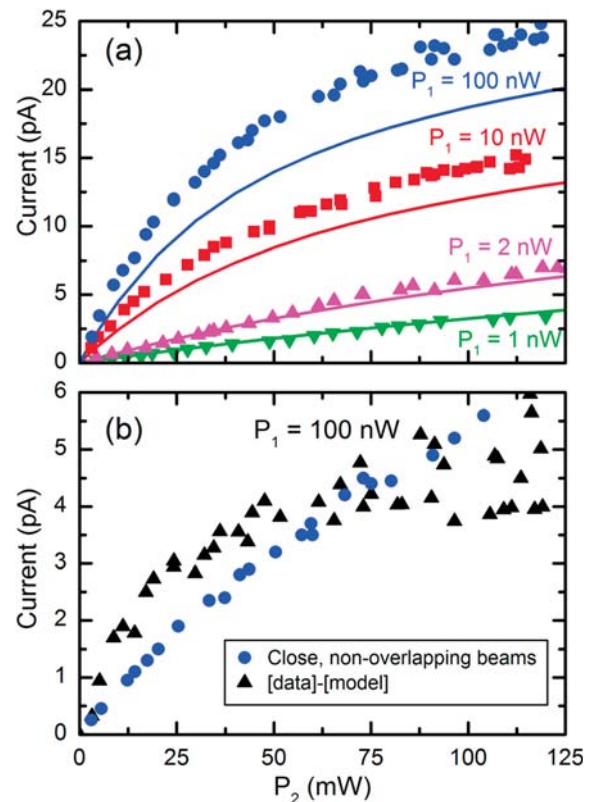


FIG. 4. (a) Measured beam currents (symbols) and model predictions (solid lines). Dependence on 508 nm laser power P_2 is shown at 852 nm laser power P_1 values of 1 nW (green, inverted triangles), 2 nW (magenta, triangles), 10 nW (red, squares) and 100 nW (blue, circles). (b) Comparison of the current collected for non-overlapping ionization beams (blue circles) with the difference between measured data and the model predictions in (a) (black triangles), indicating that rescattering is the most likely cause of the discrepancies seen at high power. Uncertainty in the current measurements is estimated to be approximately 5% (one standard deviation) of the measured value, arising predominantly from minor random variation in laser intensity and positional stability.

present. In the figure, we compare the current observed using non-overlapping beams with the difference, presumably caused by rescattering, between the overlapped-beam current and the model prediction. The agreement in both magnitude and dependence on P_2 between these two curves strongly suggests that rescattering is the dominant cause of the discrepancy observed in Figure 4(a).

Because for some applications, such as rapid milling of large volumes of material, it is more important to have a high beam current than a high brightness, we performed tests to determine the maximum current achievable with our current realization of the source. We found that by defocusing the photoionization lasers we could overlap a larger volume of the atomic beam and produce significantly more current. In this configuration we found that the source was able to produce over 5 nA of total current, albeit at a reduced brightness. This beam current is significantly higher than sources based on MOTs have been able to produce to date.

V. COULOMB INTERACTIONS

The effects of inter-ion forces are an important consideration for an ion source with the high level of brightness predicted

by our estimates. As previously described in the literature^{14,27} the presence of multiple ions near the source region can result in collisions and consequent heating, which can substantially reduce the ion beam's brightness. Using higher extraction electric fields can ameliorate this problem; however the beam's energy spread is proportional to the extraction field, and a larger energy spread will cause more chromatic aberrations in the FIB's final lens, resulting in a larger spot size.

By comparison with the LMIS, which can have current densities as high as⁴ 10^{10} A m^{-2} , resulting in behavior dominated by Coulomb interactions, the cold atomic beam ion source current density of 0.16 A m^{-2} is extremely low. Nevertheless, because the ions are accelerated more gradually over a longer distance, the effects of inter-ion forces can be significant. Even in cases where these effects do not substantially reduce the peak brightness, the forces may induce substantial deviations from a thermal velocity distribution. In the focal plane this will result in a non-Gaussian current distribution, which may contain beam "tails" extending far beyond the nominal spot size.

In order to investigate whether Coulomb repulsive effects in our ion source would degrade brightness, and in turn lead to an increase in focal spot size, we performed a series of Monte-Carlo simulations. The simulations used the software developed for a previous publication.²⁷ This software incorporates all of the pairwise Coulomb forces between simulated ions and calculates their trajectories as they are accelerated by a constant electric field. As a starting point we generate ions in a Poissonian random process with a three-dimensional spatial distribution $P(x, y, z)$ as calculated in the model described above. Particles are then accelerated in a 100 kV/m field over a distance of 10 mm . At the end of the acceleration, $z = a$, the peak current density $J(0, 0, a)$ and the temperature of the beam defined as $T = m(\sigma_{v_x}^2 + \sigma_{v_y}^2)/2k_B$ are calculated and used with Eq. (5) to determine a peak brightness value. For the cases considered, correlation between transverse velocity and position was not large enough to significantly affect the calculated brightness.

To highlight the effects of Coulomb interactions, we consider sub-populations of the particles which have transverse velocities less than a specific value, and plot the brightness of these sub-populations as a function of the fraction of the total beam they represent. Thus the brightness at a fraction close to one represents the brightness of almost the entire beam, including nearly all the particles that have large transverse velocities due to Coulomb collisions, while the brightness corresponding to a smaller fraction is the brightness of those particles that had fewer Coulomb interactions. We note that the distribution of velocities created from the Coulomb interactions is non-Gaussian; as a result, the brightness inferred from the simulation output may be dominated by a small fraction of ions that are most affected by Coulomb interactions. Plotting the brightness as a function of beam fraction gives a clearer picture of how the source-limited spot size in a real column will be impacted by inter-ion forces. This method of presentation is similar to the one used in Ref. 14.

Figure 5 shows the ion beam brightness as function of beam fraction at several achievable currents. The solid lines

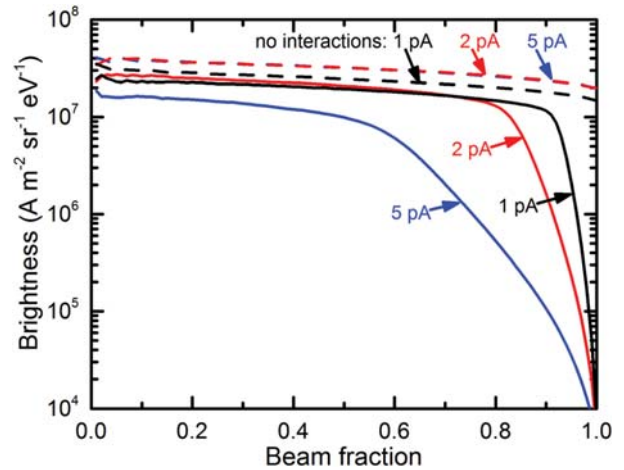


FIG. 5. Monte Carlo calculations of peak brightness as a function of beam fraction for a variety of beam currents and ionization geometries. Solid lines indicate calculations for currents of 1 pA (black), 2 pA (red), and 5 pA (blue) with all Coulomb interactions included. For comparison, dashed lines show calculations without Coulomb interactions (note the 5 pA curve is indistinguishable from the 2 pA curve). Initial velocities were chosen to be commensurate with a temperature of $30 \mu\text{K}$. Initial ion positions were calculated using distributions generated by Eq. (11) with experimentally realistic input parameters, given in Tables I and II. The acceleration field was 100 kV/m .

represent calculations performed with all Coulomb interactions taken into account. For comparison, the dotted lines indicate the same calculations performed with Coulomb interactions turned off. For these calculations, the integrated atom flux F , the atom beam width σ_A , the saturation intensity I_s , the atomic beam velocity v , and the ionization cross section σ_{ion} were chosen according to the experimental conditions shown in Table I. The laser beam powers and sizes $\{P_1, \sigma_1, P_2, \sigma_2\}$ were adjusted in each case to yield the desired total current, with the constraint that they be experimentally tractable, i.e., $\sigma_{1,2} \geq 1 \mu\text{m}$, $P_1 < 2 \text{ nW}$, and $P_2 \leq 125 \text{ mW}$. The values chosen for each calculation are given in Table II. We note that for the 2 pA and 5 pA cases, the peak current density was equal to that achieved with the experimental conditions specified in Table I (0.16 A m^{-2}), while for the 1 pA case, the peak current density was slightly lower (0.12 A m^{-2}).

As seen in the figure, the 1 pA beam shows little effect from Coulomb interactions, maintaining high brightness for over 90% of the total beam. Most of the 2 pA beam is also minimally affected by Coulomb interactions, with only 20% showing a substantially reduced brightness. At the higher current of 5 pA, the brightness is still large, but Coulomb interactions do have a significant effect, even at small beam fractions. Increasing the extraction field will mitigate the

TABLE II. Laser powers P_1, P_2 and beam radii σ_1, σ_2 used for the calculations of the three beam currents shown in Figure 5. Also shown is the peak current density $J_{\text{ion}}(0, 0, +\infty)$.

Beam current (nA)	P_1 (nW)	P_2 (mW)	σ_1 (μm)	σ_2 (μm)	$J_{\text{ion}}(0, 0, +\infty)$ (A m^{-2})
1	0.07	90	1.0	1.0	0.12
2	0.16	125	1.0	1.1	0.16
5	0.75	125	1.5	1.75	0.16

effects of Coulomb interactions on brightness; however, operation at higher currents will necessarily involve optimizing the resulting tradeoff between brightness and energy spread. The results for a 2 pA beam imply that inter-ion interactions should not substantially reduce the beam's brightness below $1 \times 10^7 \text{ A m}^{-2} \text{ sr}^{-1} \text{ eV}^{-1}$ for the beam geometry and extraction electric field examined here.

VI. SPOT SIZE ESTIMATE

Using a brightness value of $1 \times 10^7 \text{ A m}^{-2} \text{ sr}^{-1} \text{ eV}^{-1}$ and an energy spread of 0.34 eV, we calculate an estimate of the spot size that could be achievable with the present source if it were used in conjunction with a typical focusing column. Choosing representative values for the beam current I , the focal plane convergence angle α , the spherical aberration coefficient C_s , and the chromatic aberration coefficient C_c , we employ the formula derived by Barth and Kruit²⁸

$$d_{50} = [(d_{\text{br}}^{1.3} + d_{\text{sph}}^{1.3})^{2/1.3} + d_{\text{chr}}^2]^{1/2}, \quad (13)$$

where d_{50} is the diameter into which 50% of beam's current would fall, $d_{\text{br}} = (2/\pi)\sqrt{I/(BE_0)}\alpha^{-1}$ is the spot size contribution from the brightness, $d_{\text{sph}} = (1/2)^{5/2}C_s\alpha^3$ is the contribution from spherical aberration, and $d_{\text{chr}} = 0.34 C_c\alpha\Delta E/E_0$ is the contribution from chromatic aberration. This formula predicts that the present system will be able to focus 1 pA with a d_{50} of less than 0.7 nm at a beam energy of 30 keV if we assume spherical and chromatic coefficients of 100 mm and 30 mm, respectively, and a focal plane convergence angle of 2.2 mrad, a value chosen such that it minimizes Eq. (13).

VII. CONCLUSIONS

The high brightness and low energy spread predicted for this new cold atomic beam ion source compare very favorably with the LMIS and GFIS sources used today. No fundamental limits of the present system have been identified so far, and a number of refinements could be implemented to further improve performance. Brightness could be increased by improving the optical molasses cooling stage; temperatures below 10 μK in cesium²⁹ should be achievable. Further refinements to the 2D^+ -MOT beam-forming stage would yield higher total atom fluxes. With such a system spot sizes below 0.5 nm may be achievable. The source should be capable of addressing some larger scale milling tasks as well, considering that it may also be used in a high current, lower brightness mode of operation, as evidenced by our observation of over 5 nA emission.

Additional measurements need to be performed before any firm predictions of system performance can be made. First, a direct measurement of the energy spread of the ion beam would serve to further validate the model. Also, a characterization of any heating that occurs during the conversion from cold atoms to ions is vitally important. A direct test of the system brightness would serve this purpose, but this will be a challenge owing to the very low emittance of the ion beam. Finally there remain a number of technical challenges, such as the design of an ion acceleration column and focusing column which can accelerate the beam to full energy without reducing

its brightness. This column will also need to adjust the beam diameter to achieve the optimal opening angle in the final focusing lens. We anticipate that further refinements and more testing of this new and promising ion source will allow for a more complete picture of the system's capabilities to emerge.

ACKNOWLEDGMENTS

B.K. and A.V.S. acknowledge support under the Cooperative Research Agreement between the University of Maryland and the National Institute of Standards and Technology Center for Nanoscale Science and Technology, Grant No.70NANB10H193, through the University of Maryland and from the National Science Foundation under Grant No. 1248521.

- ¹L. A. Giannuzzi and F. A. Stevie, *Introduction to Focused Ion Beams: Instrumentation, Theory, Techniques, and Practice* (Springer, 2005).
- ²J. M. Chabala, K. K. Soni, J. Li, K. L. Gavrilov, and R. Levi-Setti, *Int. J. Mass Spectrom. Ion Process.* **143**, 191 (1995).
- ³L. Scipioni, L. A. Stern, J. Notte, S. Sijbrandij, and B. Griffin, *Adv. Mater. Process.* **166**, 27 (2008).
- ⁴C. W. Hagen, E. Fokkema, and P. Kruit, *J. Vac. Sci. Technol. B* **26**, 2091 (2008).
- ⁵L. W. Swanson, G. A. Schwind, and A. E. Bell, *J. Appl. Phys.* **51**, 3453 (1980).
- ⁶B. W. Ward, J. A. Notte, and N. P. Economou, *J. Vac. Sci. Technol. B* **24**, 2871 (2006).
- ⁷B. G. Freinkman, A. V. Eletsii, and S. I. Zaitsev, *Microelectron. Eng.* **73–74**, 139 (2004).
- ⁸B. J. Claessens, S. B. van der Geer, G. Taban, E. J. D. Vredendregt, and O. J. Luiten, *Phys. Rev. Lett.* **95**, 164801 (2005).
- ⁹J. L. Hanssen, J. J. McClelland, E. A. Dakin, and M. Jacka, *Phys. Rev.* **74**, 063416 (2006).
- ¹⁰B. J. Claessens, M. P. Reijnders, G. Taban, O. J. Luiten, and E. J. D. Vredendregt, *Phys. Plasmas* **14**, 093101 (2007).
- ¹¹J. L. Hanssen, S. B. Hill, J. Orloff, and J. J. McClelland, *Nano Lett.* **8**, 2844 (2008).
- ¹²A. V. Steele, B. Knuffman, J. J. McClelland, and J. Orloff, *J. Vac. Sci. Technol. B* **28**, C6F1 (2010).
- ¹³B. Knuffman, A. V. Steele, J. Orloff, and J. J. McClelland, *New J. Phys.* **13**, 103035 (2011).
- ¹⁴S. B. van der Geer, M. P. Reijnders, M. J. de Loos, E. J. D. Vredendregt, P. H. A. Mutsaers, and O. J. Luiten, *J. Appl. Phys.* **102**, 094312 (2007).
- ¹⁵M. Senoner and W. E. S. Unger, *J. Anal. At. Spectrom.* **27**, 1050 (2012).
- ¹⁶J. Nellessen, J. Werner, and W. Ertmer, *Opt. Commun.* **78**, 300 (1990).
- ¹⁷C. C. Tsao, Y. Wang, J. Weiner, and V. S. Bagnato, *J. Appl. Phys.* **80**, 8 (1996).
- ¹⁸J. G. C. Tempelaars, R. J. W. Stas, P. G. M. Sebel, H. C. W. Beijerinck, and E. J. D. Vredendregt, *Eur. Phys. J. D* **18**, 113 (2002).
- ¹⁹K. Dieckmann, R. J. C. Spreeuw, M. Weidemüller, and J. T. M. Walraven, *Phys. Rev.* **58**, 3891 (1998).
- ²⁰Z. T. Lu, K. L. Corwin, M. J. Renn, M. H. Anderson, E. A. Cornell, and C. E. Wieman, *Phys. Rev. Lett.* **77**, 3331 (1996).
- ²¹H. J. Metcalf and P. van der Straten, *Laser Cooling and Trapping* (Springer, New York, 1999).
- ²²All uncertainties in this paper are intended to be interpreted as one-standard-deviation, combined standard uncertainty (n.d.).
- ²³*Springer Handbook of Atomic, Molecular, and Optical Physics*, 2nd ed., edited by G. W. F. Drake (Springer, 2005).
- ²⁴P. W. Hawkes and E. Kasper, *Principles of Electron Optics* (Academic Press, 1996), Vol. 2.
- ²⁵O. Maragò, D. Ciampini, F. Fuso, E. Arimondo, C. Gabbanini, and S. T. Manson, *Phys. Rev.* **57**, R4110 (1998).
- ²⁶B. M. Patterson, T. Takekoshi, and R. J. Knize, *Phys. Rev.* **59**, 2508 (1999).
- ²⁷A. V. Steele, B. Knuffman, and J. J. McClelland, *J. Appl. Phys.* **109**, 104308 (2011).
- ²⁸J. E. Barth and P. Kruit, *Optik* **101**, 101 (1996).
- ²⁹M. Drewsen, P. Laurent, A. Nadir, G. Santarelli, A. Clairon, Y. Castin, D. Grison, and C. Salomon, *Appl. Phys. B: Lasers Opt.* **59**, 283 (1994).